

See discussions, stats, and author profiles for this publication at: <https://www.researchgate.net/publication/257308516>

Mass-Based Photothermal Comparison Among Gold Nanocrystals, PbS Nanocrystals, Organic Dyes, and Carbon Black

ARTICLE *in* THE JOURNAL OF PHYSICAL CHEMISTRY C · APRIL 2013

Impact Factor: 4.77 · DOI: 10.1021/jp400770x

CITATIONS

14

READS

90

5 AUTHORS, INCLUDING:



Ruibin Jiang

The Chinese University of Hong Kong

29 PUBLICATIONS 792 CITATIONS

SEE PROFILE



Si Cheng

Soochow University (PRC)

23 PUBLICATIONS 294 CITATIONS

SEE PROFILE



Lei Shao

Chalmers University of Technology

28 PUBLICATIONS 932 CITATIONS

SEE PROFILE

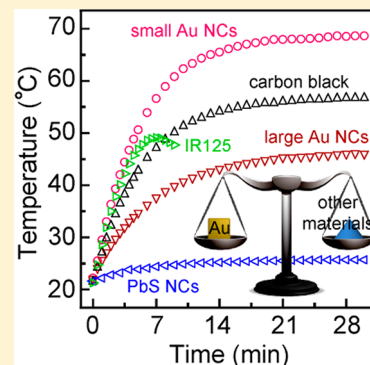
Mass-Based Photothermal Comparison Among Gold Nanocrystals, PbS Nanocrystals, Organic Dyes, and Carbon Black

Ruibin Jiang, Si Cheng, Lei Shao, Qifeng Ruan, and Jianfang Wang*

Department of Physics, The Chinese University of Hong Kong, Shatin, Hong Kong SAR, China

S Supporting Information

ABSTRACT: Gold nanocrystals have attractive plasmon-enabled photothermal conversion properties, which have been widely employed for photothermal therapy and solar energy harvesting. For practical applications, the mass-normalized photothermal conversion performance is often desired to be known for Au nanocrystals with different shapes and sizes and for different nanomaterials. We study the photothermal conversion performances of differently shaped and sized Au nanocrystals and compare them with those of PbS nanocrystals, carbon black, and organic dyes at the same mass concentrations. Both the mass-normalized extinction cross section and the photothermal conversion efficiency of Au nanocrystals decrease as their size is increased. The photothermal conversion performance of carbon black is comparable to that of relatively small Au nanocrystals, while the photothermal conversion performance of organic dyes and PbS nanocrystals is inferior to that of Au nanocrystals. Our results are useful for the design of Au nanocrystals and the choice of nanomaterials for photothermal applications.



Gold nanocrystals can support localized surface plasmon resonances (LSPRs), which are the collective oscillations of the electrons in the conduction band. Their LSPR wavelengths can be tailored from the visible to infrared regions by synthetically varying their size and shape.¹ Their extinction cross sections are larger than those of other optical species, such as atoms, ions, organic dyes, and quantum dots, even if the cross sections are normalized against the physical dimensions of the different optical species.² When LSPRs are excited, they can bring extremely strong electric field enhancements to the vicinity of plasmonic Au nanocrystals. The large field enhancements and scattering cross sections of Au nanocrystals have been employed in chemical and biomedical sensing,^{3–6} biomedical imaging,^{6–8} plasmon-enhanced spectroscopies, such as Raman and fluorescence,^{2,9–12} photocatalysis,^{13,14} and solar cells.^{15–17} On the other hand, the large absorption cross sections enable Au nanocrystals to show distinguished photothermal conversion properties. The photothermal conversion of Au nanocrystals has been utilized for the killing of cancer cells and bacteria,^{7,8,18,19} the delivery of genes and drugs,^{20,21} optical data storage,²² microfluidic heating,^{23,24} nanoscale patterning,²⁵ and photothermal microscopy.^{26–28}

Many works have been carried out to investigate the photothermal conversion properties of Au nanocrystals.^{29–34} These studies focused mainly on the characterization and understanding of the photothermal conversion efficiencies of differently shaped and sized Au nanocrystals. Our previous study made on differently sized Au nanocrystals has revealed that the photothermal conversion efficiency increases when the nanocrystal size is reduced.³⁴ The photothermal heating performance of an ensemble Au nanocrystal sample is jointly determined by the photothermal conversion efficiency and the total extinction value at the laser illumination wavelength. The

variation of the photothermal conversion efficiency with the nanocrystal size has already been understood. The total extinction value, on the other hand, is proportional to the product of the extinction cross section of the individual Au nanocrystal and the particle concentration. At a fixed metal mass concentration, both the particle concentration and the extinction cross section of the individual Au nanocrystal vary with the nanocrystal shape and size. Understanding the photothermal conversion performance of differently shaped and sized Au nanocrystals at fixed mass concentrations will be of critical importance for future large-scale practical applications based on plasmonic photothermal conversion, because the cost of a material is usually closely related to its mass. To date, the mass-based comparison of the photothermal conversion performance has rarely been made among different Au nanocrystals. To the best of our knowledge, there has been only one report on the photothermal conversion performance of differently sized Au nanocrystals at the same Au mass concentration.³³ In that study, the Au nanocrystals have a pyramidal shape and are polycrystalline. They were fabricated by first preparing pyramidal pits on (100) Si substrates through masked etching and then depositing gold through evaporation. The LSPRs of polycrystalline metal nanostructures fabricated by evaporation methods have been shown to be severely damped owing to the electron scattering at numerous grain boundaries.^{35,36} In addition, the photothermal conversion measurements in that study were performed under off-resonance excitation conditions. Photothermal conversion

Received: January 23, 2013

Revised: March 29, 2013

Published: April 9, 2013



under on-resonance excitation conditions has been known to be very different from that under off-resonance excitation conditions. A small deviation of the excitation wavelength from the LSPR wavelength can give a large change in the photothermal conversion efficiency.^{27,34}

In this work, we studied the photothermal conversion performance of five different Au nanocrystal samples at the same Au mass concentration. The LSPR wavelengths of the five samples were synthetically controlled to be the same. The photothermal conversion studies were carried out under on-resonance excitation conditions. We further compared the photothermal conversion performance of the Au nanocrystals with that of organic dyes, carbon black, and PbS nanocrystals under both laser illumination and solar radiation. Organic dyes are often used in photothermal cancer therapy. Carbon black and PbS are two types of common materials widely used in various industries for absorbing sunlight and converting it into heat. Our results will be useful for practical applications based on photothermal conversion.

Five differently sized Au nanocrystal samples were prepared to study the dependence of the photothermal conversion performance on the nanocrystal size. They are three Au nanorod (Au NR) samples and two Au nanobipyramid (Au NBP) samples. Au NBP samples were used because it has been difficult to grow high-quality Au NR samples that are comparable to Au NBPs in size and have longitudinal plasmon resonance wavelengths around 809 nm. The Au NRs were prepared using a seed-mediated growth method together with anisotropic shortening.¹ The Au NBPs were prepared by seed-mediated growth together with transverse overgrowth.^{37,38} Our previous study has shown that the highest temperature reached at the thermal steady state is obtained when the LSPR wavelength of Au nanocrystals is equal to the illumination laser wavelength.³⁴ The longitudinal plasmon wavelengths of the five elongated Au nanocrystal samples were therefore all synthetically tailored to be 809 nm, which is the wavelength of the semiconductor laser used in our experiments. The transmission electron microscopy (TEM) images of the five samples are given in Figure 1A–E. The extinction spectra normalized against the longitudinal plasmon resonance peak are shown in Figure 1F. The TEM images and narrow extinction spectra clearly reveal that the sizes of the Au NRs and NBPs are uniform. Besides NRs and NBPs, there are also nearly spherical nanocrystals in the samples. The longitudinal plasmon peak of the Au NR samples at 809 nm is much stronger than the transverse one at 511 nm, which is in agreement with our previous results^{1,34,37} and suggests that the number yields of Au NRs in these samples are above 95%. The number yields of Au NBPs in the two samples are relatively low. They are in the range 40–55%.

The photothermal conversion properties of each Au nanocrystal sample were first studied at different concentrations. The wavelength of the illumination laser was 809 nm. The laser power was fixed at 1.72 W. The concentrations were monitored by measuring the extinction spectra. The extinction spectra and temperature rise traces under the laser illumination for the medium Au NR sample at five different concentrations are provided in Figure 1G,H. The data for the other four Au nanocrystal samples are given in Figure S1 in the Supporting Information. The temperatures of all the samples are seen to increase rapidly under the laser illumination. The nanocrystal solutions reach their steady-state temperatures within ~15 min. The extinction values at the longitudinal plasmon peak and the

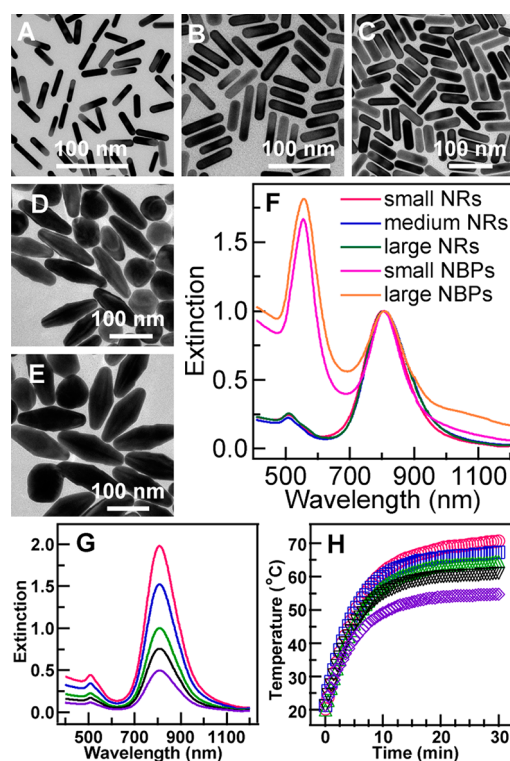


Figure 1. (A–E) TEM images of the five differently sized Au nanocrystal samples. Their average lengths/diameters are $(36 \pm 3)/(10 \pm 1)$, $(60 \pm 9)/(16 \pm 2)$, $(70 \pm 7)/(20 \pm 4)$, $(127 \pm 10)/(49 \pm 2)$, and $(154 \pm 11)/(61 \pm 4)$ nm, respectively. The diameters of the Au NBPs were measured at the middle. (F) Normalized extinction spectra of the five Au nanocrystal samples. (G) Extinction spectra of the medium Au NR sample at five different concentrations. (H) Temperature rise traces of the medium Au NR sample at different concentrations under the laser illumination. The trace is plotted in the same color as the extinction spectrum for each concentration.

corresponding steady-state temperatures of all the five samples at different concentrations are listed in Table S1 in the Supporting Information.

The photothermal conversion efficiency was determined according to the thermal balance, as described in our previous report.³⁴ The energy output was determined by switching off the laser after the nanocrystal solution reached the steady state and measuring the temperature decay curve. We found that the temperature decay curves of each Au nanocrystal sample at different concentrations can collapse into one curve by shifting the time axis. Therefore, only one temperature decay curve for each Au nanocrystal sample is provided in Figure S2 in the Supporting Information. The obtained photothermal conversion efficiencies of each sample at different concentrations are given in Table S2 in the Supporting Information. Figure 2A shows that both the steady-state temperatures and the photothermal conversion efficiencies of all the Au nanocrystal samples increase as the extinction values at the longitudinal plasmon resonance peak are increased. The increase in the steady-state temperature with the extinction value at the longitudinal plasmon peak can be readily understood as resulting from the increase in the absorbed light energy as the extinction value is raised. In contrast, the photothermal conversion efficiency should be independent of the extinction value for a given Au nanocrystal sample. In addition, the change of the photothermal conversion efficiency with the extinction

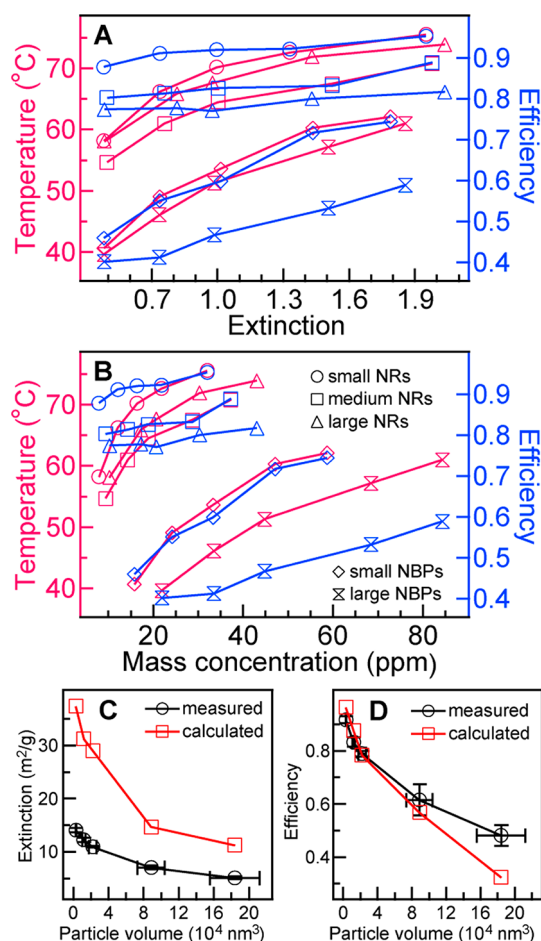


Figure 2. (A) Steady-state temperature (left axis) and photothermal conversion efficiency (right axis) of the five Au nanocrystal samples versus the extinction value at the longitudinal plasmon resonance peak. (B) Steady-state temperature (left axis) and photothermal conversion efficiency of the five samples versus the Au mass concentration. (C, D) Mass-normalized extinction cross section and photothermal conversion efficiency versus the particle volume, respectively. The symbols in part A refer to the same samples as those in part B.

value is also found to become more distinct as the nanocrystal size is increased. This counterintuitive phenomenon can be rationalized by considering the scattering and reabsorption of Au nanocrystals in solutions, as discussed below.

The steady-state temperatures and photothermal conversion efficiencies were next studied as functions of the Au mass concentration for each nanocrystal sample (Figure 2B). The Au mass concentrations were measured using inductively coupled

plasma mass spectrometry (ICP-MS). For a given Au nanocrystal sample, both the steady-state temperature and the photothermal conversion efficiency increase as the Au mass concentration is increased. At a given Au mass concentration, smaller Au nanocrystals give higher steady-state temperatures and possess higher photothermal conversion efficiencies. Therefore, if the Au mass concentration is the same, the photothermal conversion performance improves as the nanocrystal size is reduced.

The photothermal conversion performance is determined by the extinction value at the illumination laser wavelength and the conversion efficiency. The extinction value is linearly proportional to the particle concentration as well as the Au mass concentration. In order to better compare the extinction values of differently sized Au nanocrystals at the same Au mass concentration, we define a parameter, which is called the mass-normalized extinction cross section, $\sigma_{\text{ext,m}}$. $\sigma_{\text{ext,m}}$ is calculated by multiplying together the number of nanocrystals per unit mass and the extinction cross section of a single nanocrystal. The extinction cross section of a single nanocrystal can be determined by either experimental measurements or numerical simulations. Experimentally, the extinction cross section σ_{ext} of a single nanocrystal can be determined according to

$$\varepsilon = \frac{N\sigma_{\text{ext}}l}{2.303} \quad (1)$$

where ε is the extinction value at a given wavelength, N is the particle concentration, and l is the optical path length. The extinction value can be obtained by measuring the extinction spectrum. The particle concentration can be estimated from the Au mass concentration measured with ICP-MS and the average nanocrystal size measured with TEM imaging. For the Au NBP samples, since a considerable fraction of Au nanospheres is present, the number yield of Au NBPs was estimated from the TEM images. The obtained number yields of the small and large Au NBP samples are 42.9% and 52.8%, and the corresponding mass percentages of Au NBPs after the particle volumes of the Au nanocrystals being taken into account are 42.1% and 52.4%, respectively. The absorption, scattering, and extinction cross sections can also be obtained numerically by the finite-difference time-domain (FDTD) method. Since the orientations of Au nanocrystals in solutions are random, the calculated cross sections were corrected for the random orientations according to the previously reported method so that the measured and calculated cross sections can be better compared.^{32,39}

Table 1 summarizes the particle cross sections and the mass-normalized extinction cross sections obtained from the experimental measurements and FDTD simulations for the

Table 1. Particle Volumes, Optical Cross Sections, and Photothermal Conversion Efficiencies of the Differently Sized Au Nanocrystals

Au nanocrystal sample	particle volume (1000 nm ³)	calculated					measured		
		$\sigma_{\text{ext}} (10^{-15} \text{ m}^2)$	$\sigma_{\text{scat}}^a (10^{-15} \text{ m}^2)$	$\sigma_{\text{abs}}^b (10^{-15} \text{ m}^2)$	$\sigma_{\text{ext,m}} (\text{m}^2 \text{ g}^{-1})$	η^c	$\sigma_{\text{ext}} (10^{-16} \text{ m}^2)$	$\sigma_{\text{ext,m}} (\text{m}^2 \text{ g}^{-1})$	η
small Au NRs	2.8 ± 0.6	6.1	0.2	5.9	37.4	0.96	7.7 ± 0.4	14.1 ± 0.7	0.92 ± 0.03
medium Au NRs	12 ± 3	21.8	2.7	19.1	31.3	0.88	29 ± 2	12.2 ± 0.8	0.83 ± 0.03
large Au NRs	22 ± 9	37.0	7.9	29.1	29.0	0.78	46 ± 1	10.9 ± 0.3	0.79 ± 0.02
small Au NBPs	89 ± 31	75.4	32.6	42.8	14.7	0.57	120 ± 13	7.0 ± 0.8	0.6 ± 0.1
large Au NBPs	184 ± 57	119.8	81.0	38.8	11.2	0.32	180 ± 19	5.1 ± 0.5	0.48 ± 0.08

^a σ_{scat} refers to the scattering cross section. ^b σ_{abs} refers to the absorption cross section. ^c η is the photothermal conversion efficiency.

differently sized Au nanocrystal samples. The calculated and measured $\sigma_{\text{ext,m}}$ values both decrease as the particle volume is increased (Figure 2C). However, the measured $\sigma_{\text{ext,m}}$ values are smaller than the calculated ones. This discrepancy can be attributed mainly to the inhomogeneous size distributions in the Au nanocrystal samples. In the FDTD simulations, σ_{ext} of an averagely sized Au nanocrystal was calculated at its longitudinal plasmon resonance wavelength for each sample. In the experiments, the longitudinal plasmon resonance maxima of the Au nanocrystals with sizes different from the average one are shifted away from the extinction peak of the ensemble sample. The extinction cross section of a Au nanocrystal is a function of the wavelength. It has a maximal value at the plasmon resonance peak and decreases as the wavelength gets either longer or shorter than the plasmon resonance wavelength. Therefore, the inhomogeneous size distributions cause the measured extinction cross sections to be smaller than the calculated ones. This factor has also been recognized in previous studies.³⁹

FDTD simulations can also give the photothermal conversion efficiency, which is simply the ratio between the absorption and extinction cross sections. We first verified by FDTD simulations that the shape difference between the Au NR and NBP samples has little effect on the photothermal conversion efficiency. We considered a Au NR that is 20-nm wide and 70-nm long and has a longitudinal plasmon wavelength of 804 nm and a Au NBP that is 22-nm wide at the waist and 86-nm long and has a longitudinal plasmon wavelength of 810 nm. The two nanocrystals have the same particle volume. The extinction cross section and photothermal conversion efficiency of the NR are $3.7 \times 10^{-14} \text{ m}^2$ and 0.79, respectively. The corresponding values of the NBP are $4.0 \times 10^{-14} \text{ m}^2$ and 0.77, respectively. The difference in their extinction cross sections is smaller than 10%, and the photothermal conversion efficiencies are nearly the same. We then calculated the photothermal conversion efficiencies of the different Au nanocrystal samples. Both the measured and calculated photothermal conversion efficiencies are also listed in Table 1. For a Au nanocrystal with a given size, only one photothermal conversion efficiency value can be obtained from FDTD simulations. However, in the experiments, the photothermal conversion efficiency is found to depend on the nanocrystal concentration. To better compare the dependence of the photothermal conversion efficiency on the particle volume between the experiments and simulations, we take the averages of the photothermal conversion efficiencies at different particle concentrations. Figure 2D shows clearly that the photothermal conversion efficiency decreases as the particle volume is increased. The calculated photothermal conversion efficiencies are in good agreement with the experimental ones when the particle volume is small. However, when the particle volume gets larger, the calculated value becomes smaller than the measured one. This difference between the experiments and calculations is ascribed to the reabsorption of the scattered light among the Au nanocrystals in the ensemble sample of the experiments. The reabsorption of the scattered light causes the measured conversion efficiencies to be larger than the calculated ones. The reabsorption effect gets larger with increasing nanocrystal sizes, because larger Au nanocrystals have higher scattering cross sections. Since both $\sigma_{\text{ext,m}}$ and the photothermal conversion efficiency decrease with increasing particle volumes, the photothermal conversion performance, as reflected by the steady-state temperature, at the same mass

concentration becomes worse as the particle volume is increased (Figure 2B). In addition, the increase in the measured photothermal conversion efficiency with increasing particle concentrations (Figure 2A and B) can also be attributed to the reabsorption effect, because the scattering of light gets stronger if more Au nanocrystals are present in solutions.

As mentioned above, there have been a number of studies on the photothermal conversion properties of variously shaped Au nanocrystals. However, to date, to the best of our knowledge, there have been no studies on comparing the photothermal conversion performance of Au nanocrystals with that of other nanomaterials. We therefore further investigated the photothermal conversion properties of PbS nanocrystals, carbon black, and two organic dyes and compared them with those of the Au nanocrystal samples. PbS is a direct band gap semiconductor with a band gap energy of 0.41 eV. The PbS nanocrystal sample was prepared according to a previous report.⁴⁰ Scanning electron microscopy (SEM) imaging shows that the PbS nanocrystals have an octahedral shape with highly uniform sizes and shapes (Figure 3A). The carbon black was

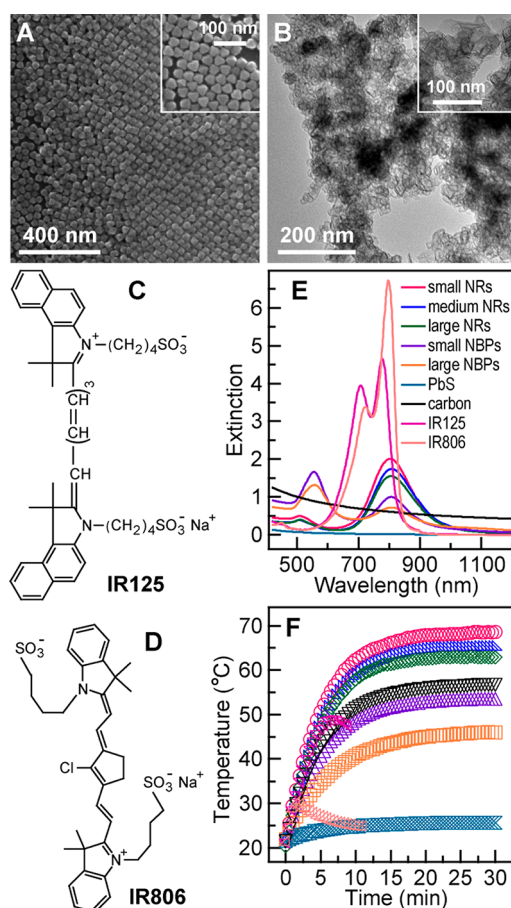


Figure 3. (A) SEM image of the PbS nanocrystals. The inset is an enlarged image. The average diameter, measured by approximating each PbS nanocrystal as a sphere, is $(32 \pm 2) \text{ nm}$. (B) TEM image of the carbon black. The inset shows an enlarged part. (C, D) Molecular structures of IR125 and IR806, respectively. (E) Extinction spectra of the different nanomaterials at the same mass concentration of 32.8 ppm in water. (F) Temperature rise traces of the different nanomaterials under the laser illumination at the same mass concentration of 32.8 ppm. The different colors in part F represent the samples as those indicated correspondingly in part E.

Table 2. $\sigma_{\text{ext,m}}$ Values and Steady-State Temperatures of the Different Nanomaterials

	small Au NRs	medium Au NRs	large Au NRs	small Au NBPs	large Au NBPs	PbS	carbon black	IR125	IR806
$\sigma_{\text{ext,m}}^a$	14.1	12.2	10.9	7.0	5.1	0.1	4.2	13.5	38.9
T^b	68.0	65.2	61.9	53.5	46.0	25.7	56.7	49.1	30.1

^aThe mass-normalized extinction cross section values are determined at 809 nm. Their unit is $\text{m}^2 \text{g}^{-1}$. ^bThe steady-state temperatures were measured at the mass concentration of 32.8 ppm. For the two dyes, the values are the highest temperatures instead of the steady-state ones.

purchased from Cabot Corporation (EMPEROR 1800). It has a high color strength and is a water-soluble black pigment. TEM imaging shows that the carbon black is made of thin layers that are folded and entangled together (Figure 3B). Both PbS and carbon black are widely utilized in industries for absorbing sunlight and converting it into heat. The chosen organic dyes are IR125 and IR806 (Figure 3C,D). They have been widely employed for optical imaging and photothermal cancer therapy in biomedicine.^{41–43}

The photothermal conversion measurements were carried out at the same mass concentration for the Au nanocrystal, PbS nanocrystal, carbon black, and organic dye samples. Figure 3E provides the extinction spectra of all the samples at the same mass concentration of 32.8 ppm. IR125 has a major absorption peak at 778 nm and a minor absorption peak at 708 nm. IR806 has a major absorption peak at 797 nm and a minor absorption peak at 721 nm. The PbS nanocrystals and carbon black have no sharp absorption peaks. Their absorption increases gradually with decreasing wavelengths. At the wavelength of 809 nm, the extinction values are in the order of IR806 > IR125 > small Au NRs > medium Au NRs > large Au NRs > small Au NBPs > large Au NBPs > carbon black > PbS nanocrystals. The temperature rise traces of all nanomaterials under the laser illumination are plotted in Figure 3F. The steady-state temperatures are listed in Table 2 together with the mass-normalized extinction cross section values at 809 nm. For the inorganic nanomaterial samples, the steady-state temperatures are in the order of small Au NRs > medium Au NRs > large Au NRs > carbon black > small Au NBPs > large Au NBPs > PbS nanocrystals. This result indicates that the small Au nanocrystal samples have better photothermal conversion performances than the carbon black and the large Au nanocrystal samples have poorer photothermal conversion performances than the carbon black. The photothermal conversion performances of the Au nanocrystal samples are better than that of the PbS nanocrystal sample.

Another notable feature observed in Figure 3F is that both organic dyes are unstable under the laser illumination at 1.72 W. The temperatures for IR125 and IR806 first increase as functions of the illumination time. After 2 and 7 min, respectively, they start to decrease. The highest temperatures reached for IR806 and IR125 are 29.7 and 49.1 °C. In order to study the photostabilities of the two dyes, we measured the changes of the absorption spectra under the laser illumination at 0.26 and 1.72 W for IR125 and at 0.26 W for IR806 (Figure S3, Supporting Information), because the photobleaching of IR806 is very quick under the laser illumination at 1.72 W. The absorbance values for both dyes decrease rapidly as functions of time, with the decay constants on the order of minutes. This result indicates that the organic dyes are inferior to the Au nanocrystals, PbS nanocrystals, and carbon black in terms of their photostabilities.

We finally compared the photothermal conversion performances of the Au nanocrystals, PbS nanocrystals, and carbon black under solar radiation. The organic dyes were not

considered in the solar radiation study because their absorption bands are very narrow, which is not suitable for solar energy harvesting. In order to harvest solar energy as much as possible, we mixed together differently sized Au nanocrystals so that the extinction spectrum of the Au nanocrystal mixture solution can match better with the solar radiation spectrum. The Au nanocrystal mixture sample was composed of one Au nanosphere sample and nine differently sized Au NR samples. The plasmon resonance wavelength of the Au nanosphere sample is 532 nm, and the longitudinal plasmon resonance wavelengths of the nine Au NR samples are 580, 608, 632, 670, 700, 746, 798, 880, and 980 nm, respectively. A TEM image of the Au nanocrystal mixture sample is provided in Figure S4 in the Supporting Information. The extinction spectra of the Au nanocrystal mixture, PbS nanocrystals, and carbon black at the same mass concentration of 50.6 ppm are shown in Figure 4A.

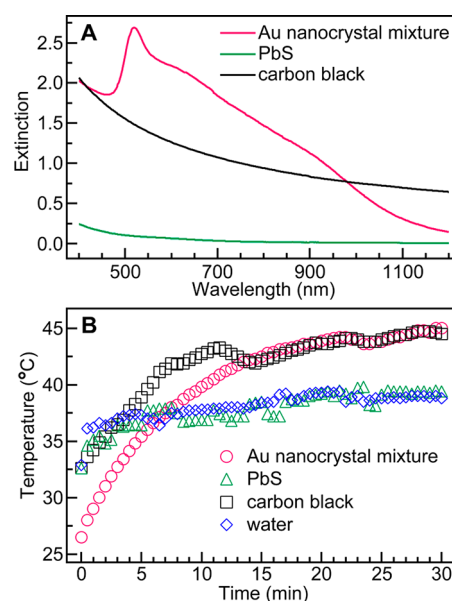


Figure 4. (A) Extinction spectra of the Au nanocrystal mixture, PbS nanocrystal sample, and carbon black at the same mass concentration of 50.6 ppm. (B) Temperature rise traces of the different nanomaterials under solar radiation at the same mass concentration of 50.6 ppm.

The extinction values of the PbS nanocrystals are smaller than those of the Au nanocrystal mixture and carbon black over the entire spectral range. Below ~1000 nm, the Au nanocrystal mixture has larger extinction values than the carbon black. Above ~1000 nm, the carbon black shows larger extinction values. We would point out that if Au NRs with longer longitudinal plasmon wavelengths could be made, Au nanocrystal mixtures could be prepared to have larger extinction values than the carbon black even at wavelengths longer than 1000 nm.

Figure 4B shows the temperature rise traces of the Au nanocrystal mixture, PbS nanocrystals, carbon black, and pure water under solar radiation. Because the optical power of sunlight was fluctuating during the photothermal measurements due to the presence of clouds on the sky (Figure S5, Supporting Information), the temperature rise traces also exhibit fluctuations. In addition, the starting temperatures vary among the different samples because each sample was measured at different time points. The final steady-state temperatures of the Au nanocrystal mixture and carbon black are 45.0 and 44.5 °C, respectively. They are nearly the same. The temperature rise trace of the PbS nanocrystals nearly overlaps with that of water, with the final steady-state temperatures clearly being lower than those of the Au nanocrystal mixture and carbon black.

In conclusion, we have studied the photothermal conversion performances of five differently sized Au nanocrystal samples, PbS nanocrystals, carbon black, and two organic dyes under laser illumination and solar radiation. The photothermal conversion efficiencies and mass-normalized extinction cross sections of Au nanocrystals decrease with increasing nanocrystal sizes. At the same mass concentration, the photothermal conversion performance of Au nanocrystals therefore decreases as the nanocrystal size is increased. Under the laser illumination, the photothermal conversion performance of the carbon black is inferior to those of the small Au nanocrystal samples but superior to those of the large Au nanocrystal samples. The photothermal conversion performances of all the Au nanocrystal samples and the carbon black are better than that of the PbS nanocrystals. The organic dyes are unstable under the laser illumination. Under solar radiation, the Au nanocrystal mixture and carbon black show similar photothermal conversion performances, and the PbS nanocrystals exhibit a poorer photothermal conversion performance. Our results will be useful not only for the design of Au nanocrystals with desired plasmonic photothermal conversion properties but also for selecting appropriate photothermal conversion nanomaterials for applications in nanomedicine and solar energy harvesting.

EXPERIMENTAL METHODS

Growth of the Au and PbS Nanocrystals. The Au nanocrystals were prepared using a seed-mediated method together with anisotropic oxidation and transverse overgrowth according to the reported procedures.^{1,37,38} The PbS nanocrystals were synthesized by a thermal decomposition method.⁴⁰ The detailed preparation procedures are described in the Supporting Information.

Characterization. The SEM imaging was performed on an FEI Quanta 400 FEG microscope. The TEM imaging was performed on an FEI Tecnai Spirit microscope operating at 120 kV. Extinction spectra were taken on a Hitachi U-3501 UV–vis–NIR spectrophotometer. The mass concentrations of the gold and lead in the Au and PbS nanocrystal solution samples were measured using a PerkinElmer Optima 4300DV ICP-MS. The setup for the measurement of the photothermal conversion was composed of a 1-cm path length quartz cuvette that was covered with a foam cap, a K-type thermocouple connected to a digital thermometer (CIE 305), a continuous semiconductor diode laser (809 nm, JUM2500/50/20, VDM00036, JENOPTIK, Germany), and a magnetic stirrer. The laser power during the measurements was 1.72 W, and the laser spot diameter was ~5 mm. The photothermal conversion under solar radiation

was performed on the roof of our four-story lab building on April 12, 2012.

FDTD Simulations. All numerical simulations were performed using a commercial software, FDTD Solutions 7.5, which was developed by Lumerical Solutions, Inc. The Au dielectric function was taken from previously measured values.⁴⁴ The Au nanocrystal and its surrounding medium were divided into meshes of 0.5 nm in size. The excitation electric field was set to be polarized along the length axis of the nanocrystal. The surrounding medium was taken as water with a refractive index of 1.333. The size and shape of the Au nanocrystal were set to be as close as possible to those measured from the TEM images. Specifically, the NR was modeled as a cylinder capped with a semisphere at each end. The NBP was modeled as two back-to-back-stacked pentapramids with their apexes truncated spherically.

ASSOCIATED CONTENT

Supporting Information

Details of the preparation procedures for the Au and PbS nanocrystals, the steady-state temperatures, photothermal conversion efficiencies, extinction spectra, and temperature rise traces of the Au nanocrystal samples at different particle concentrations, the temperature decay curves of the Au nanocrystal samples, the time-dependent absorption spectra of the organic dyes under the laser illumination, the TEM image of the Au nanocrystal mixture, and the real-time solar power density. This material is available free of charge via the Internet at <http://pubs.acs.org>.

AUTHOR INFORMATION

Corresponding Author

*E-mail: jfwang@phy.cuhk.edu.hk.

Notes

The authors declare no competing financial interest.

ACKNOWLEDGMENTS

This work was supported by Hong Kong RGC General Research Fund (No. CUHK403211, Project Code 2130277) and National Natural Science Foundation of China (No. 21229101).

REFERENCES

- (1) Ni, W. H.; Kou, X. S.; Yang, Z.; Wang, J. F. Tailoring Longitudinal Surface Plasmon Wavelengths, Scattering and Absorption Cross Sections of Gold Nanorods. *ACS Nano* **2008**, *2*, 677–686.
- (2) Ming, T.; Chen, H. J.; Jiang, R. B.; Li, Q.; Wang, J. F. Plasmon-Controlled Fluorescence: Beyond the Intensity Enhancement. *J. Phys. Chem. Lett.* **2012**, *3*, 191–202.
- (3) Mayer, K. M.; Hafner, J. H. Localized Surface Plasmon Resonance Sensors. *Chem. Rev.* **2011**, *111*, 3828–3857.
- (4) Saha, K.; Agasti, S. S.; Kim, C.; Li, X. N.; Rotello, V. M. Gold Nanoparticles in Chemical and Biological Sensing. *Chem. Rev.* **2012**, *112*, 2739–2779.
- (5) Jans, H.; Huo, Q. Gold Nanoparticle-Enabled Biological and Chemical Detection and Analysis. *Chem. Soc. Rev.* **2012**, *41*, 2849–2866.
- (6) Chen, H. J.; Shao, L.; Li, Q.; Wang, J. F. Gold Nanorods and Their Plasmonic Properties. *Chem. Soc. Rev.* **2013**, *42*, 2679–2724.
- (7) Ungureanu, C.; Kroes, R.; Petersen, W.; Groothuis, T. A. M.; Ungureanu, F.; Janssen, H.; van Leeuwen, F. W. B.; Kooyman, R. P. H.; Manohar, S.; van Leeuwen, T. G. Light Interactions with Gold Nanorods and Cells: Implications for Photothermal Nanotherapeutics. *Nano Lett.* **2011**, *11*, 1887–1894.

- (8) Bardhan, R.; Lal, S.; Joshi, A.; Halas, N. J. Theranostic Nanoshells: From Probe Design to Imaging and Treatment of Cancer. *Acc. Chem. Res.* **2011**, *44*, 936–946.
- (9) Qian, X.-M.; Nie, S. M. Single-Molecule and Single-Nanoparticle SERS: From Fundamental Mechanisms to Biomedical Applications. *Chem. Soc. Rev.* **2008**, *37*, 912–920.
- (10) Li, J. F.; Huang, Y. F.; Ding, Y.; Yang, Z. L.; Li, S. B.; Zhou, X. S.; Fan, F. R.; Zhang, W.; Zhou, Z. Y.; Wu, D. Y.; Ren, B.; Wang, Z. L.; Tian, Z. Q. Shell-Isolated Nanoparticle-Enhanced Raman Spectroscopy. *Nature* **2010**, *464*, 392–395.
- (11) Ru, E. C. L.; Grand, J.; Sow, I.; Somerville, W. R. C.; Etchegoin, P. G.; Treguer-Delapierre, M.; Charron, G.; Féridj, N.; Lévi, G.; Aubard, J. A Scheme for Detecting Every Single Target Molecule with Surface-Enhanced Raman Spectroscopy. *Nano Lett.* **2011**, *11*, 5013–5019.
- (12) Tam, F.; Goodrich, G. P.; Johnson, B. R.; Halas, N. J. Plasmonic Enhancement of Molecular Fluorescence. *Nano Lett.* **2007**, *7*, 496–501.
- (13) Hou, W. B.; Cronin, S. B. A Review of Surface Plasmon Resonance-Enhanced Photocatalysis. *Adv. Funct. Mater.* **2013**, DOI: 10.1002/adfm.201202148.
- (14) Warren, S. C.; Thimsen, E. Plasmonic Solar Water Splitting. *Energy Environ. Sci.* **2012**, *5*, 5133–5146.
- (15) Brown, M. D.; Suteewong, T.; Kumar, R. S. S.; D'Innocenzo, V.; Petrozza, A.; Lee, M. M.; Wiesner, U.; Snaith, H. J. Plasmonic Dye-Sensitized Solar Cells Using Core–Shell Metal–Insulator Nanoparticles. *Nano Lett.* **2011**, *11*, 438–445.
- (16) Ding, B.; Lee, B. J.; Yang, M. J.; Jung, H. S.; Lee, J.-K. Surface-Plasmon Assisted Energy Conversion in Dye-Sensitized Solar Cells. *Adv. Energy Mater.* **2011**, *1*, 415–421.
- (17) Wang, D. H.; Kim, D. Y.; Choi, K. W.; Seo, J. H.; Im, S. H.; Park, J. H.; Park, O. O.; Heeger, A. J. Enhancement of Donor–Acceptor Polymer Bulk Heterojunction Solar Cell Power Conversion Efficiencies by Addition of Au Nanoparticles. *Angew. Chem., Int. Ed.* **2011**, *50*, 5519–5523.
- (18) Ray, P. C.; Khan, S. A.; Singh, A. K.; Senapati, D.; Fan, Z. Nanomaterials for Targeted Detection and Photothermal Killing of Bacteria. *Chem. Soc. Rev.* **2012**, *41*, 3193–3209.
- (19) von Maltzahn, G.; Park, J.-H.; Agrawal, A.; Bandaru, N. K.; Das, S. K.; Sailor, M. J.; Bhatia, S. N. Computationally Guided Photothermal Tumor Therapy Using Long-Circulating Gold Nanorod Antennas. *Cancer Res.* **2009**, *69*, 3892–3900.
- (20) Huschka, R.; Zuloaga, J.; Knight, M. W.; Brown, L. V.; Nordlander, P.; Halas, N. J. Light-Induced Release of DNA from Gold Nanoparticles: Nanoshells and Nanorods. *J. Am. Chem. Soc.* **2011**, *133*, 12247–12255.
- (21) Fomina, N.; Sankaranarayanan, J.; Almutairi, A. Photochemical Mechanisms of Light-Triggered Release from Nanocarriers. *Adv. Drug Delivery Rev.* **2012**, *64*, 1005–1020.
- (22) Zijlstra, P.; Chon, J. W. M.; Gu, M. Five-Dimensional Optical Recording Mediated by Surface Plasmons in Gold Nanorods. *Nature* **2009**, *459*, 410–413.
- (23) Liu, G. L.; Kim, J.; Lu, Y.; Lee, L. P. Optofluidic Control Using Photothermal Nanoparticles. *Nat. Mater.* **2006**, *5*, 27–32.
- (24) Fang, C. H.; Shao, L.; Zhao, Y. H.; Wang, J. F.; Wu, H. K. A Gold Nanocrystal/Poly(dimethylsiloxane) Composite for Plasmonic Heating on Microfluidic Chips. *Adv. Mater.* **2012**, *24*, 94–98.
- (25) Cao, L. Y.; Barsic, D. N.; Guichard, A. R.; Brongersma, M. L. Plasmon-Assisted Local Temperature Control to Pattern Individual Semiconductor Nanowires and Carbon Nanotubes. *Nano Lett.* **2007**, *7*, 3523–3527.
- (26) Gaiduk, A.; Yorulmaz, M.; Ruijgrok, P. V.; Orrit, M. Room-Temperature Detection of a Single Molecule's Absorption by Photothermal Contrast. *Science* **2010**, *330*, 353–356.
- (27) Zijlstra, P.; Paulo, P. M. R.; Orrit, M. Optical Detection of Single Non-Absorbing Molecules Using the Surface Plasmon Resonance of a Gold Nanorod. *Nat. Nanotechnol.* **2012**, *7*, 379–382.
- (28) Selmke, M.; Braun, M.; Cichos, F. Photothermal Single-Particle Microscopy: Detection of a Nanolens. *ACS Nano* **2012**, *6*, 2741–2749.
- (29) Chou, C.-H.; Chen, C.-D.; Wang, C. R. C. Highly Efficient, Wavelength-Tunable, Gold Nanoparticle Based Optothermal Nanoconvertors. *J. Phys. Chem. B* **2005**, *109*, 11135–11138.
- (30) Richardson, H. H.; Hickman, Z. N.; Govorov, A. O.; Thomas, A. C.; Zhang, W.; Kordesch, M. E. Thermo-optical Properties of Gold Nanoparticles Embedded in Ice: Characterization of Heat Generation and Melting. *Nano Lett.* **2006**, *6*, 783–788.
- (31) Richardson, H. H.; Carlson, M. T.; Tandler, P. J.; Hernandez, P.; Govorov, A. O. Experimental and Theoretical Studies of Light-to-Heat Conversion and Collective Heating Effects in Metal Nanoparticle Solutions. *Nano Lett.* **2009**, *9*, 1139–1146.
- (32) Cole, J. R.; Mirin, N. A.; Knight, M. W.; Goodrich, G. P.; Halas, N. J. Photothermal Efficiencies of Nanoshells and Nanorods for Clinical Therapeutic Applications. *J. Phys. Chem. C* **2009**, *113*, 12090–12094.
- (33) Hasan, W.; Stender, C. L.; Lee, M. H.; Nehl, C. L.; Lee, J.; Odom, T. W. Tailoring the Structure of Nanopyramids for Optimal Heat Generation. *Nano Lett.* **2009**, *9*, 1555–1558.
- (34) Chen, H. J.; Shao, L.; Ming, T.; Sun, Z. H.; Zhao, C. M.; Yang, B. C.; Wang, J. F. Understanding the Photothermal Conversion Efficiency of Gold Nanocrystals. *Small* **2010**, *6*, 2272–2280.
- (35) Dittlbache, H.; Hohenau, A.; Wagner, D.; Kreibitz, U.; Rogers, M.; Hofer, F.; Aussenegg, F. R.; Krenn, J. R. Silver Nanowires as Surface Plasmon Resonators. *Phys. Rev. Lett.* **2005**, *95*, 257403.
- (36) Huang, J.-S.; Callegari, V.; Geisler, P.; Brüning, C.; Kern, J.; Prangma, J. C.; Wu, X. F.; Feichtner, T.; Ziegler, J.; Weinmann, P.; Kamp, M.; Forchel, A.; Biagioni, P.; Sennhauser, U.; Hecht, B. Atomically Flat Single-Crystalline Gold Nanostructures for Plasmonic Nanocircuitry. *Nat. Commun.* **2010**, *1*, 150.
- (37) Kou, X. S.; Zhang, S. Z.; Yang, Z.; Tsung, C.-K.; Stucky, G. D.; Sun, L. D.; Wang, J. F.; Yan, C. H. Glutathione- and Cysteine-Induced Transverse Overgrowth on Gold Nanorods. *J. Am. Chem. Soc.* **2007**, *129*, 6402–6404.
- (38) Kou, X. S.; Ni, W. H.; Tsung, C.-K.; Chan, K.; Lin, H.-Q.; Stucky, G. D.; Wang, J. F. Growth of Gold Bipyramids with Improved Yield and Their Curvature-Directed Oxidation. *Small* **2007**, *3*, 2103–2113.
- (39) Muskens, O. L.; Bachelier, G.; Fatti, N. D.; Vallée, F.; Brioude, A.; Jiang, X. C.; Pileni, M.-P. Quantitative Absorption Spectroscopy of a Single Gold Nanorod. *J. Phys. Chem. C* **2008**, *112*, 8917–8921.
- (40) Zhao, Z. H.; Zhang, K.; Zhang, J. H.; Yang, K.; He, C. Z.; Dong, F. X.; Yang, B. Synthesis of Size and Shape Controlled PbS Nanocrystals and Their Self-Assembly. *Colloid Surf., A* **2010**, *355*, 114–120.
- (41) Skirtach, A. G.; Antipov, A. A.; Shchukin, D. G.; Sukhorukov, G. B. Remote Activation of Capsules Containing Ag Nanoparticles and IR Dye by Laser Light. *Langmuir* **2004**, *20*, 6988–6992.
- (42) Yu, J.; Javier, D.; Yaseen, M. A.; Nitin, N.; Richards-Kortum, R.; Anvari, B.; Wong, M. S. Self-Assembly Synthesis, Tumor Cell Targeting, and Photothermal Capabilities of Antibody-Coated Indocyanine Green Nanocapsules. *J. Am. Chem. Soc.* **2010**, *132*, 1929–1938.
- (43) Zheng, X. H.; Xing, D.; Zhou, F. F.; Wu, B. Y.; Chen, W. R. Indocyanine Green-Containing Nanostructure as Near Infrared Dual-Functional Targeting Probes for Optical Imaging and Photothermal Therapy. *Mol. Pharmaceutics* **2011**, *8*, 447–456.
- (44) Johnson, P. B.; Christy, R. W. Optical Constants of the Noble Metals. *Phys. Rev. B* **1972**, *6*, 4370–4379.

Supporting Information

Mass-Based Photothermal Comparison among Gold Nanocrystals, PbS Nanocrystals, Organic Dyes, and Carbon Black

*Ruibin Jiang, Si Cheng, Lei Shao, Qifeng Ruan, and Jianfang Wang**

Department of Physics, The Chinese University of Hong Kong, Shatin, Hong Kong SAR, China

1. Growth of the Gold Nanocrystals with the Same Longitudinal Plasmon Wavelength

The seed-mediated method was employed together with the anisotropic oxidation and transverse overgrowth to grow the Au NRs and NBPs with the same longitudinal plasmon wavelength but different sizes in aqueous solutions. Deionized water was used for all the preparations. For the growth of the Au NRs, the seed solution was made by the addition of freshly prepared, ice-cold NaBH_4 (0.6 mL, 0.01 M) into a mixture composed of HAuCl_4 (0.25 mL, 0.01 M) and cetyltrimethylammonium bromide (CTAB, 9.75 mL, 0.1 M). The seed solution was kept at room temperature for 2 h before use. The growth solution was prepared by the sequential addition of HAuCl_4 (2 mL, 0.01 M), AgNO_3 (0.4 mL, 0.01 M), HCl (0.8 mL, 1.0 M), and ascorbic acid (0.32 mL, 0.1 M) into CTAB (40 mL, 0.1 M). After the resultant solution was mixed by swirling for 30 s, 0.08 mL of the seed solution was injected. The reaction solution was gently inversion-mixed for 2 min and then left undisturbed overnight. The obtained Au NRs have an ensemble longitudinal plasmon wavelength of 810 nm and are denoted as the large NRs. The growth procedure described above was also used to prepare the Au NRs with longitudinal plasmon wavelengths of 850 and 886 nm by changing the volume of the seed solution from 0.08 to 0.3 and 0.5 mL, respectively.

The obtained Au NR samples with longitudinal wavelengths of 850 and 886 nm were subjected to oxidation by adding an appropriate amount of HAuCl_4 (0.01 M). The amount of added HAuCl_4 was adjusted according to the oxidation process. The plastic tubes containing the Au NR solutions were transferred into an isothermal oven at 45 °C. The oxidation process was monitored by measuring the extinction spectra of the NR solutions from time to time. When the longitudinal plasmon wavelength reached ~810 nm, the oxidation process was stopped by centrifuging the NR samples and then redispersing them in water. The Au NRs obtained from the sample with a longitudinal plasmon wavelength of 850 nm were denoted as the medium NRs, and the Au NRs oxidized from the sample with a longitudinal plasmon wavelength of 886 nm were named as the small NRs.

Citrate-stabilized seeds were employed for the growth of the Au NBPs. For the seed preparation, HAuCl_4 (0.125 mL, 0.01 M) and sodium citrate (0.25 mL, 0.01 M) were first added to water (9.625 mL), followed by the addition of freshly prepared, ice-cold solution of NaBH_4 (0.15 mL, 0.01 M) under vigorous stirring. The resultant seed solution was kept at room temperature for 2 h before use. The growth solution was made by the sequential addition of HAuCl_4 (1.2 mL, 0.01 M), ascorbic acid (0.402 mL, 0.1 M), and AgNO_3 (0.06 mL, 0.01 M) into cetyltributylammonium bromide (CTBAB, 28.5 mL, 0.01 M). The seed solution (0.10 or 0.20 mL) was then added to the growth solution, followed by gentle inversion mixing for 10 s. The resultant solution was left undisturbed overnight in an isothermal oven at 65 °C. The Au NBP samples obtained from 0.10 and 0.20 mL of the seed solution have ensemble longitudinal plasmon wavelengths of 1121 and 997 nm, respectively. The small and large Au NBPs were respectively prepared by overgrowth from the Au NBPs with longitudinal plasmon wavelengths of 997 and 1121 nm. The overgrowth solution was made by mixing together CTAB (42.75 mL, 0.1 M), HAuCl_4 (1.8 mL, 0.01 M), AgNO_3 (0.27 mL, 0.01 M), and ascorbic acid (0.288 mL, 0.1 M). Before overgrowth, a glutathione solution (0.15 mL, 0.01 M) was added into 15 mL of the pre-grown NBP solution. After the resultant NBP solution was kept at room temperature for 2 h, 25 mL of the overgrowth solution was added. The overgrowth process was monitored by recording the extinction spectra from time to time. When the longitudinal plasmon wavelength reached ~810 nm, the obtained NBPs were washed by centrifugation and redispersed in water.

2. Growth of the Gold Nanocrystals for the Preparation of the Mixture Solution

The Au nanocrystal samples utilized to prepare the mixture solution for solar photothermal conversion were also grown by combining the seed-mediated method together with anisotropic shortening. The Au NR samples with longitudinal plasmon wavelengths of 532, 580, 608, 632, 670, 700, 746, 798, and 880 nm were produced by the aforementioned oxidation method from the Au NR sample with a longitudinal plasmon wavelength of 886 nm. The Au NR sample with a longitudinal plasmon wavelength of 886 nm was grown by using the aforementioned seed-mediated method. The Au NR sample with a longitudinal plasmon wavelength of 980 nm was also made by the aforementioned seed-mediated method with slight modification. Briefly, CTBAB (1.0 mL, 0.1 M) was introduced into the growth solution, the volume of the added seed solution was 0.15 mL, and the other conditions were kept the same.

3. Growth of the PbS Nanocrystals

For the growth of the PbS nanocrystals, an aqueous thioacetamide solution (10.22 mL, 0.5 M) was added into the aqueous mixture of CTAB (2.57 mL, 0.1 M), acetic acid (4.10 mL, 1 M), and lead acetate (10.22 mL, 0.1 M) at room temperature. The mixture was subsequently heated to 80 °C and kept at this temperature for 8 h. After reaction, the resultant black precipitate was purified by two cycles of centrifugation and redispersion into water.

Table S1. Steady-State Temperatures (T) of Each Au Nanocrystal Sample at Different Concentrations and Therefore Different Extinction Values (E) at 809 nm

Au nanocrystal sample										
	E	T (°C)	E	T (°C)	E	T (°C)	E	T (°C)	E	T (°C)
small NRs	1.950	75.5	1.329	72.6	0.996	70.2	0.735	66.2	0.479	58.4
medium NRs	1.978	70.8	1.521	67.5	1.002	64.5	0.758	61.0	0.496	54.7
large NRs	2.035	73.9	1.430	71.9	0.975	67.6	0.814	65.9	0.482	58.1
small NBPs	1.788	62.1	1.434	60.3	1.014	53.6	0.735	49.1	0.479	40.7
large NBPs	1.856	61.0	1.505	57.2	0.984	51.3	0.734	46.1	0.481	39.7

Table S2. Photothermal Conversion Efficiencies (η) of Each Au Nanocrystal Sample at Different Concentrations and Therefore Different Extinction Values (E) at 809 nm

Au nanocrystal sample										
	E	η	E	η	E	η	E	η	E	η
small NRs	1.950	0.95	1.329	0.92	0.996	0.92	0.735	0.91	0.479	0.88
medium NRs	1.978	0.89	1.521	0.83	1.002	0.83	0.758	0.81	0.496	0.80
large NRs	2.035	0.82	1.430	0.80	0.975	0.77	0.814	0.78	0.482	0.78
small NBPs	1.788	0.75	1.434	0.72	1.014	0.60	0.735	0.55	0.479	0.46
large NBPs	1.856	0.67	1.505	0.60	0.984	0.52	0.734	0.45	0.481	0.41

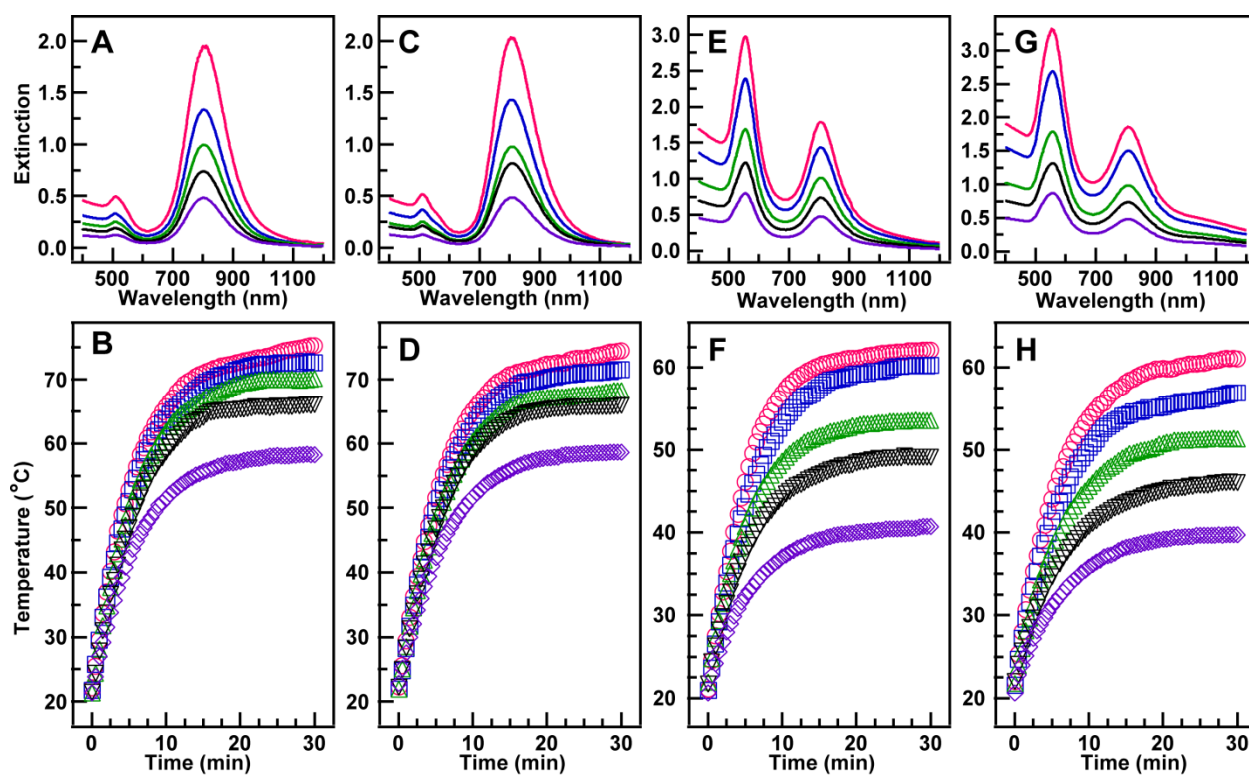


Figure S1. Extinction spectra (upper row) and temperature rise traces under laser illumination for the small Au NRs (A,B), large Au NRs (C,D), small Au NBPs (E,F), and large Au NBPs (G,H) at different concentrations, respectively.

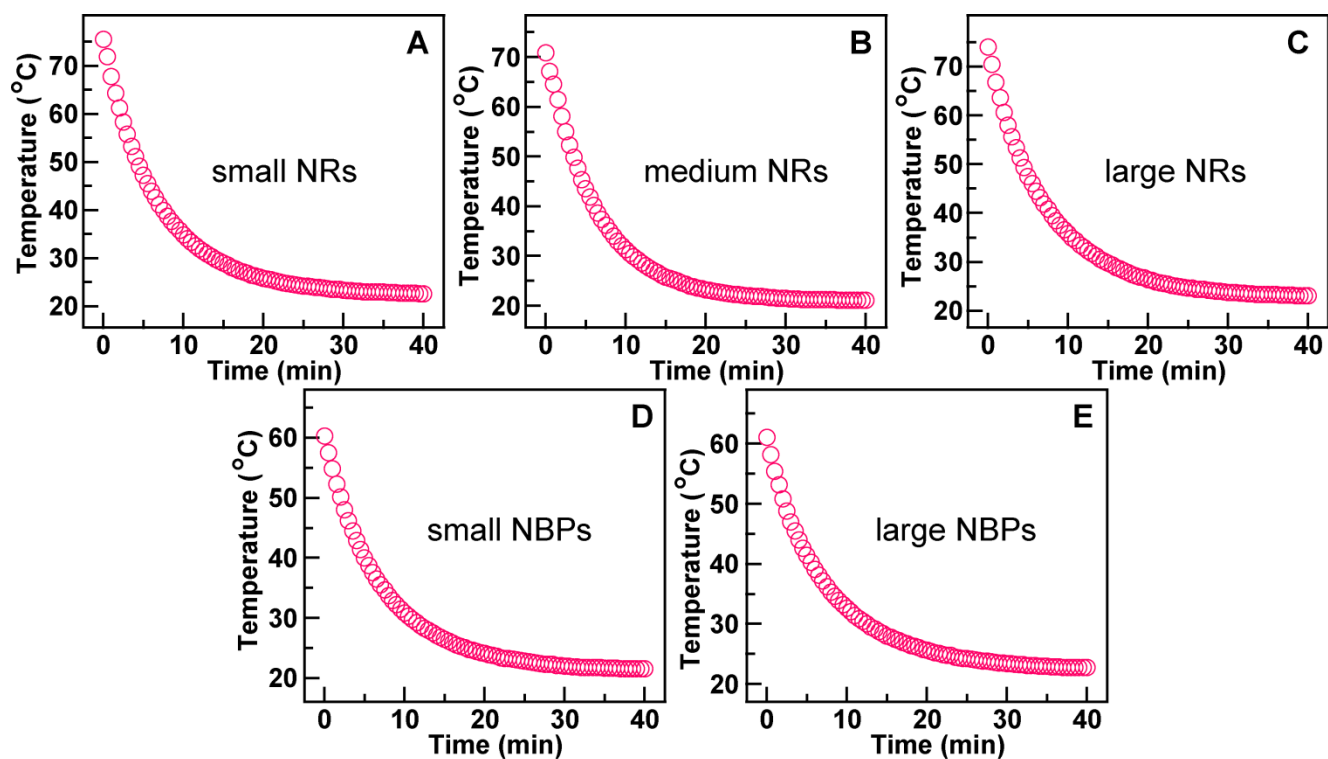


Figure S2. Temperature-decay curves for the (A) small Au NRs, (B) medium Au NRs, (C) large Au NRs, (D) small Au NBPs, and (E) large Au NBPs.

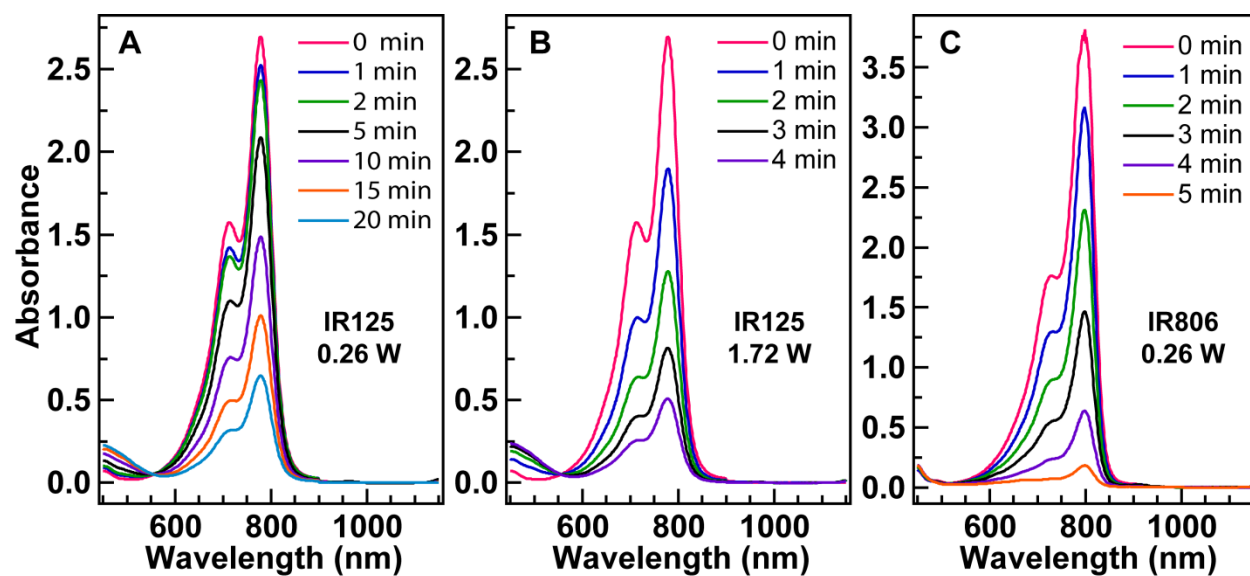


Figure S3. Evolution of the absorption spectra of IR125 and IR806 as functions of the laser illumination time.

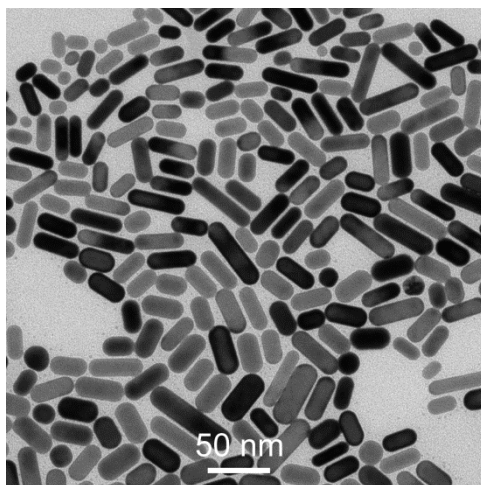


Figure S4. TEM image of the Au nanocrystal mixture for solar photothermal conversion.

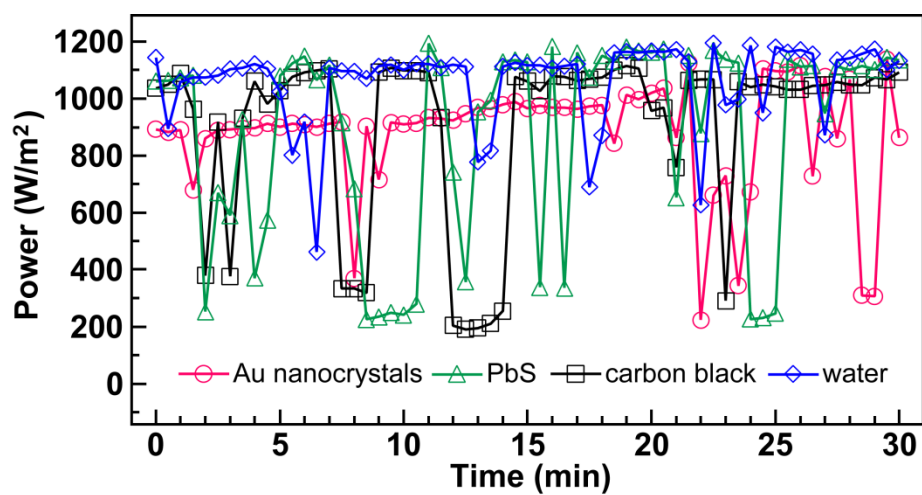


Figure S5. Solar power fluctuations as functions of time during the solar photothermal measurements.